Author(s): Tanttu, Joni; Harjupatana, Tero; Miettinen, Arttu; Kataja, Markku

Title: Monitoring semi-free swelling and water transport in bentonites using X-ray radiography

Year: 2024

Version: Published version

Please cite the original version:

Tanttu, J., Harjupatana, T., Miettinen, A., & Kataja, M. (2024). Monitoring semi-free swelling and water transport in bentonites using X-ray radiography. Applied Clay Science, 256, Article 107443. https://doi.org/10.1016/j.clay.2024.107443

Research Paper

Monitoring semi-free swelling and water transport in bentonites using X-ray radiography

Joni Tanttu [*], Tero Harjupatana, Arttu Miettinen, Markku Kataja

Department of Physics and Nanoscience Center, University of Jyväskylä, P.O. Box 35 (YFL), FI-40014 Jyväskylä, Finland

A B S T R A C T

Clay materials such as montmorillonite-rich bentonite, are planned to be used as buffer materials between waste canisters and host rock in deep geological radioactive waste repositories. To ensure the safety of the repository over very long time scales, it is essential to understand the mechanical and transport properties of the clay materials through measurements and modelling. Here, an experimental method based on X-ray radiography was used to gather temporal data on the hydro-mechanical behaviour and homogenisation of three bentonites with different initial dry densities and wetting solution chemistry. The results showed that the salinity of wetting solution and the dominant cation of montmorillonite affect the overall saturation and swelling process of the clay material thus indicating that there is a chemical coupling to the hydro-mechanical behaviour of montmorillonite-rich clay materials. In particular, higher salinity was associated with more rapid wetting and a more homogeneous distribution of bentonite material in the final state of the experiments. The results also highlighted that the new measurement method is much faster and less cumbersome than traditional gravimetric methods. The method yielded detailed data on the wetting and swelling processes, and may thus help obtain better insight on the intricate hydro-mechanical properties of clay materials.

1. Introduction

Water transport and deformation due to changing water content in the pore structure of materials are extensively studied phenomena in many fields of material science and technology such as in soil mechanics, biology and construction engineering (Markgraf et al., 2006; Pereira et al., 2009; Alaoui et al., 2011; Fanta et al., 2014). Often, these hydro-mechanical processes are complex and their modelling requires estimation of several parameters, and validation using experimental data. Clay materials, e.g. bentonite and its main component montmorillonite are prime examples of complex materials with intricate wetting properties. Due to the mineralogical and chemical structure of montmorillonite, bentonite can swell considerably when exposed to moisture. The properties of bentonite clay have been studied both theoretically and experimentally to gain an understanding of its behaviour when used as a buffer material in deep geological nuclear waste repositories (Karnland et al., 2008; Ye et al., 2010; Yustres et al., 2017; Kröhn, 2019).

The density homogenisation of bentonite buffer containing voids (e. g. installation gaps between bentonite blocks or voids between bentonite pellets) or other density heterogeneities has been a much studied topic

recently. Ideally, such voids are filled with wetting and swelling bentonite and the heterogeneous density distribution becomes homogeneous over time. However, previous studies have indicated that the dry density distribution at full saturation, even after a long period of time, may not be homogeneous. Too large density differences might compromise the performance of the buffer, and hence understanding the homogenisation process is important. For example, Dueck et al. (2019) conducted experiments on MX-80 bentonite homogenisation with varied geometries employing extensive system modelling. They observed that dry density gradients evolve slowly, with higher initial dry density leading to higher swelling pressures. Similarly, Daniels et al. (2021) explored homogenisation of MX-80 bentonite, but under elevated temperatures and varied void expansion lengths. The main observations were that elevated temperatures speed up the homogenisation process in MX-80 bentonite, but the dry density gradients persist at the end of the experiments. Villar et al. (2023) studied FEBEX bentonite, analysing void swelling, water content, and dry density evolution over time using vapour and water saturation tests, and also employed multiple sample sets with varying experiment durations. They reported heterogeneous, slow-evolving dry density and water content profiles in FEBEX

* Corresponding author.
  E-mail address: joni.a.tanttu@jyu.fi (J. Tanttu).

bentonite. Daniels et al. (2024) conducted swelling and homogenisation experiments on sodium-based MX-80 and calcium-based KJ-II bentonites, wetted with high salinity NaCl solutions (1 M and 3 M). Their conclusion was that higher salinity resulted in faster homogenisation and decreased peak swelling pressures in MX-80 bentonite.

In the above studies, the homogenisation of wetted bentonite samples was studied by monitoring swelling pressures at different locations of samples or by applying the gravimetric method (Gardner, 1986) (weighing sample before and after oven drying to obtain water content and dry density) to sliced samples at the end of the experiments. In the former method, the pressure sensors allow continuous monitoring but provide only indirect information about the mechanical behaviour. The gravimetric method produces relative accurate data on the dry density and water content distributions but as a destructive method it is impractical for measuring the detailed spatio-temporal wetting and swelling behaviour in bentonite samples. Multiple non-invasive 2D and 3D imaging methods based on nuclear magnetic resonance, electromagnetic radiation and particle radiation have been utilized for studying water transport in porous materials (Gummerson et al., 1979; Nizovtsev et al., 2008; Tippkötter et al., 2009; Zhang et al., 2011). Despite the large number of available measurement methods, not many of them are suitable for measuring time-dependent water content and material deformation at the same time. Additionally, some of the imaging methods mentioned above, e.g. neutron radiography, are not readily available, particularly for longer studies where experiments lasting several months are required.

An experimental non-invasive method for measuring deformation and water transport in swelling materials using X-ray tomography was introduced by Harjupatana et al. (2015). The method was used to study bentonite samples in constant volume conditions and was able to provide displacement field and water content in three spatial dimensions as a function of time. In many cases, such as the case of free initial swelling of bentonite, the swelling process can be quite fast. For example, in the present study the fastest swelling rate was approximately 1.8 mm/min. For comparison, a tomography scan done with the kind of equipment used, e.g. by Harjupatana et al. (2015) typically takes around 45 min. Capturing adequate tomographic images in a fast process requires high-speed tomography mainly available in synchrotron facilities (Wildenschild and Sheppard, 2013). To facilitate the study of such processes using tabletop devices based on X-ray tube sources, the original tomographic method was recently modified to be applicable in X-ray radiography by Harjupatana et al. (2022). The basic method includes sequential X-ray radiography with repeated correction radiograph acquisition for local beam hardening correction, essential for quantitative radiography. Image analysis together with careful calibration yields local deformation, and solid and water content distributions at different points in time. The X-ray radiographic method is limited to more simple geometrical set-ups but is faster than the original tomographic technique since at each time step only a single radiograph instead of a full tomographic scan is required. With the method, the time evolution of deformation and water content distribution in a material sample can be measured also during rapid wetting and free swelling. The method is applicable for essentially one and two-dimensional processes as well as for three-dimensional processes with well-defined symmetry.

In this paper, a stable and robust measurement set-up for monitoring the swelling of clay materials in limited free space was assembled to study the chemical coupling to the hydro-mechanical behaviour of clay materials. The method previously used to measure non-constrained free swelling and erosion of clay buffer in Harjupatana et al. (2022) is now applied, for the first time, to study the homogenisation process of similar materials in a more constrained semi-free swelling set-up. This set-up featured a sample holder that allowed essentially one-dimensional wetting and swelling of cylindrical samples in the axial direction. Three different clay materials, two different initial dry densities and seven wetting solutions of different chemical compositions and salinities were used in the experiments. The effect of salinity was of particular interest as the salinity is known to affect the wetting and swelling behaviour and the groundwater salinity at the disposal site may change over time. The method offers distinct advantages by providing time series information on the homogenisation process of a single sample, rather than relying solely on the initial and final states of the sample or gathering temporal information from a set of multiple samples. The research aims to enhance the understanding of bentonite behaviour by capturing and presenting detailed time series data during the homogenisation process in a semi-free swelling experiment. The modifications made to the method enabled the recording of intricate data on the rapid, chemically coupled swelling of different clay materials in a constrained swelling environment, using widely available and easily accessible equipment.

In essence, the detailed data generated by the study serves as a valuable resource for furthering the understanding of the hydro-mechanical behaviour of clay materials in conditions involving limited void space. This emphasis on detailed data collection and analysis constitutes the primary novelty of the research. The data can be used, e. g. to support the modelling of the clay buffer behaviour and the safety analysis of the used nuclear fuel repository concepts.

2. Materials and methods

2.1. Materials and samples

Three different clay materials were studied in the present work: commercial Wyoming bentonite (CWB) BARA-KADE® (Bentonite Performance Minerals LLC, Houston, Texas), supplied by B + Tech Oy, Finland, and purified sodium montmorillonite (PSM) and purified calcium montmorillonite (PCM), both supplied by Clay Technology AB, Sweden (Table 1). The initial water content values of the supplied CWB, PSM and PCM materials were 7.2%, 3.2% and 11.3%, measured gravimetrically (oven drying at 105 °C for 24 h). In order to facilitate the preparation and handling of samples, especially those made of very fine-grained PSM and PCM powders, the initial water content of the materials was increased to 14–20% by keeping powder at a relative humidity of 100% until the mass gain corresponded the desired water content. Each clay material was also doped with 1.0 wt% of 0.3 mm diameter zirconium dioxide (ZrO_2) spheres to facilitate deformation measurement. Cylindrical samples of diameter 20 mm and height 11 mm were uniaxially compacted from powdery clay materials using a die and two punches. The final compaction to a height of 10 mm was performed in a sample chamber (see Sect. 2.2) to seal the lateral surface of the sample against the chamber wall. Two different initial dry densities of the samples (1.4 g/cm^3 and 1.8 g/cm^3) were used in the experiments. In addition, the composition of the wetting solution was varied between the experiments. The CWB samples were wetted with saline solutions of three different ionic strengths. These salinities correspond the estimated minimum and maximum groundwater salinities, and their average, at the Olkiluoto nuclear waste repository in Finland during the early evolution period of 1000 years. The PSM and PCM samples were wetted with corresponding homoionic solutions (NaCl for PSM and CaCl2 for PCM) of two different ionic strengths to avoid cation exchange. Each solution was prepared by dissolving proper amounts of NaCl and CaCl2 in distilled water. All the material combinations used in the experiments are shown in Table 2. Each experiment was repeated three times.

2.2. Sample chamber

The sample chambers were designed to hold cylindrical clay samples in a closed space, where wetting and semi-free swelling were controlled and monitored (Fig. 1). A sample was kept inside an aluminium tube between two porous sintered glass filter discs (pore diameter 10–16 μm). The tube was closed with two plugs sealed against the walls with lubricated O-rings. These plugs enabled monitoring of swelling pressure using force sensors (Button Load Cell 3136_0, Phidgets Inc., capacity 1.6

Table 1

Mineralogical and various other properties of the studied clay materials: commercial Wyoming bentonite (CWB), purified sodium montmorillonite (PSM), and purified calcium montmorillonite (PCM). CWB was characterised by B + Tech Oy, but the structural formula is from an older batch (Kiviranta and Kumpulainen, 2011). PSM and PCM were characterised by Clay Technology AB.

	CWB	PSM	PCM
Mineralogical composition [wt%]			
montmorillonite	83.9	95.4	94.4
quartz	6.2	4.0	4.5
plagioclase	3.2		
K-feldspar	1.9		
gypsum	1.3		
pyrite	1.2		
calcite	1.1		
cristobalite	0.7	0.6	1.1
illite/mica	0.4		
anatase	0.2		
Montmorillonite structural formula	$Na^+_{0.46}Ca^{2+}_{0.19}Mg^{2+}_{0.07}$	$Na^+_{0.73}Ca^{2+}_{0.01}K^+_{0.02}$	$Na^+_{0.01}Ca^{2+}_{0.36}K^+_{0.01}$
	$(Si_{7.91}Al_{0.09})$	$(Si_{7.73}Al_{0.27})$	$(Si_{7.76}Al_{0.24})$
	$(Al_{3.11}Fe^{3+}_{0.35}Fe^{2+}_{0.03}Mg_{0.47})$	$(Al_{3.06}Ti_{0.01}Fe^{3+}_{0.41}Mg_{0.53})$	$(Al_{3.08}Ti_{0.01}Fe^{3+}_{0.38}Mg_{0.53})$
	$O_{20}(OH)_4$	$O_{20}(OH)_4$	$O_{20}(OH)_4$
Cation exchange capacity [eq/kg]	0.86	0.97	0.88
Grain density [g/cm^3]	2.78		

Table 2

Material combinations used in experiments. The columns $c(Na^+)$, $c(Ca^{2+})$ and $c(Cl^-)$ are the concentrations of individual ions in the aqueous solution. All the experiments listed here were repeated three times.

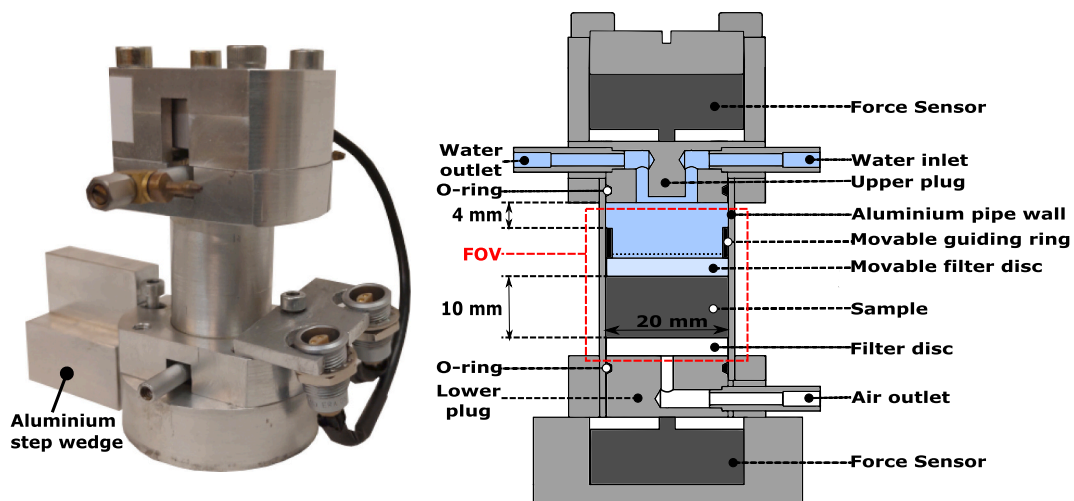| Exp. ID	Material	Initial dry density [g/cm^3]	Initial water content	$c(Na+)$ [mM]	$c(Ca^{2+})$ [mM]	$c(Cl^-)$ [mM]	Ionic strength [mM]
E1	CWB	1.4	0.14	1.95	0.525	3.0	3.5
E2	CWB	1.4	0.14	271	72.9	416.5	489
E3	CWB	1.4	0.14	540	145	830	975
E4	CWB	1.8	0.14	1.95	0.525	3.0	3.5
E5	CWB	1.8	0.14	271	72.9	416.5	489
E6	CWB	1.8	0.14	540	145	830	975
E7	PSM	1.4	0.19	975	0	975	975
E8	PSM	1.8	0.19	3.5	0	3.5	3.5
E9	PCM	1.4	0.20	0	325	650	975
E10	PCM	1.8	0.20	0	1.17	2.33	3.5

Fig. 1. Photograph (left) and schematic illustration of sample chamber (right) used in semi-free swelling experiments. The red dashed rectangle represents the approximate field of view (FOV) of the X-ray radiograph, in which wetting and swelling processes were monitored (see examples of radiographs in Fig. 3). (For interpretation of the references to colour in this figure legend, the reader is referred to the web version of this article.)

MPa and accuracy 6 kPa in the present set-up) at both ends. The water was introduced into the chamber through an inlet channel, to the space between the upper filter disc and the upper plug, and finally into the sample through the upper filter disc. Excess water and possible air bubbles were removed through a water outlet channel. The sample was able to expand axially upwards approximately 4 mm, after which a guiding ring became in contact with the upper plug. At this point, the free swelling phase ended and the further wetting and swelling were constrained in a constant volume. The total duration of each experiment was 16 days, around four times longer than the time after which the radiographs indicated the sample was fully saturated and the homogenisation process progressed very slowly. The lower filter disc was fixed

against the lower plug, which included an open channel for releasing pore air, but also allowed water vapour and, in principle, liquid water to be released from the sample. However, no liquid water was observed in the channel during the experiments. An aluminium step wedge, used to obtain correction radiographs for local beam hardening correction (Harjupatana et al., 2022), was placed next to the base of the sample chamber. The chamber was mounted to linear stages which allowed to focus the desired region of the sample and the step wedge in the field of view by horizontal and vertical movements.

2.3. X-ray radiographic method

The original radiographic method (Harjupatana et al., 2022) is briefly summarized in this section. The method is based on taking consecutive X-ray radiographs of the sample during the wetting and swelling process. The images are first corrected using the local beam hardening correction (LBHC) to correct spatio-temporal artefacts caused by beam hardening and various detector and source instabilities. The corrected radiographs are then converted into linear attenuation coefficient (LAC) distributions by applying the Beer-Lambert law pixel-wise in a form

$$\mu = -\frac{1}{x} \cdot ln\frac{I}{I_0}, \tag{1}$$

where I/I_0 is the transmittance through the sample of thickness x. When assuming negligible X-ray attenuation in the gas phase, the LAC of a partially saturated sample can be written as

$$\mu = \nu_s \cdot \rho_s + \nu_w \cdot \rho_w, \tag{2}$$

where ν_s and ν_w are the mass attenuation coefficients (MACs) and ρ_s and ρ_w are the partial densities of solid and water, respectively. The MACs are obtained through density calibration, i.e. fitting Eq. (2) to at least two calibration points (see Sect. 2.5).

The deformation of the sample is measured by applying an image correlation algorithm (e.g. block-matching) to the reference and deformed state radiographs. For sufficient image correlation, the sample should contain natural or added details, visible in radiographs.

The main results (partial densities) for a cylindrical sample and one-dimensional wetting geometry are calculated by first dividing the sample virtually into cylindrical layers, whose boundaries follow the motion of solid material according to the measured deformation. The partial densities of solid and water in layer j are given by

$$\rho_{s,j}(t) = \frac{h_j(t_{ref})}{h_j(t)} \cdot \rho_{s,j}(t_{ref}) \tag{3}$$

and

$$\rho_{w,j}(t) = \frac{\mu_j(t) - \nu_s \cdot \rho_{s,j}(t)}{\nu_w}, \tag{4}$$

where h_j is the height of layer j and t_{ref} refers to the reference state, which is typically the initial state ($t_{ref} = t_0$). The only unknown is thus the partial density of solid in the reference state $\rho_{s,j}(t_{ref})$, which can be calculated by combining the definition of the (gravimetric) water content $w = \rho_w/\rho_s$ and Eq. (2) yielding

$$\rho_{s,j}(t_{ref}) = \frac{\mu_j(t_{ref})}{\nu_s + \nu_w \cdot w_j(t_{ref})}. \tag{5}$$

For this study, the method was modified to suit present experimental needs, and these changes will be discussed next in Sects. 2.4, 2.5 and 2.6.

2.4. Forward-backward analysis

The image correlation algorithm used here (block-matching) is best suited for small deformations, requiring a dense enough field of details representative of the material displacement. In this study, the large and rapid deformation associated with the initial free swelling of clay samples compromised the accuracy of the algorithm. The resulting inaccuracies at the beginning of the experiment propagated forward in time and resulted in non-physical partial density fluctuations at later times, especially in the top layers of the sample where the deformation was large.

This problem was reduced by performing the deformation measurement and the density analysis also backwards in time, i.e. by using the final state as the reference state ($t_{ref} = t_f$) and proceeding towards the initial state. By assuming that the sample was fully saturated in the final state, the partial densities of solid and water in layer j were calculated as

$$\rho_{s,j}(t_f) = \frac{\mu(t_f) - \nu_w \cdot \widetilde{\rho}_w}{\nu_s - \nu_w \cdot \widetilde{\rho}_w / \widetilde{\rho}_s} \tag{6}$$

and

$$\rho_{w,j}(t_f) = \widetilde{\rho}_w \cdot \left(1 - \frac{\rho_{s,j}(t_f)}{\widetilde{\rho}_s}\right), \tag{7}$$

where $\widetilde{\rho}_w$ and $\widetilde{\rho}_s$ are the intrinsic densities of water and solid phases, respectively ($\widetilde{\rho}_s$ is also called grain density). The partial densities in the previous states were then calculated using Eqs. (3) and (4).

The backward analysis reduced density fluctuations between initial and final states, which were primarily caused by the cumulative error in the image correlation due to the initial rapid swelling of clay material. A combination of analysis directions was done by using the forward analysis for the initial swelling and then switching to the backward analysis when the partial densities started to fluctuate. The criterion for the switch between the analysis direction depended on the swelling rate. Samples with slower swelling speed used the forward analysis longer and faster swelling samples relied more on the backward analysis and the switch was done at an earlier phase of the experiment.

2.5. Density calibration

To take advantage of Eqs. (2) to (7), the MACs of water and solid must be known. As the compositions of solid and water varied between the experiments, each sample was calibrated separately. The MACs were defined by fitting Eq. (2) to three calibration points shown in Fig. 2, and using them as free parameters. The three calibration data points were the average values of ρ_s, ρ_w and μ of 1) the sample in the initial state, 2)
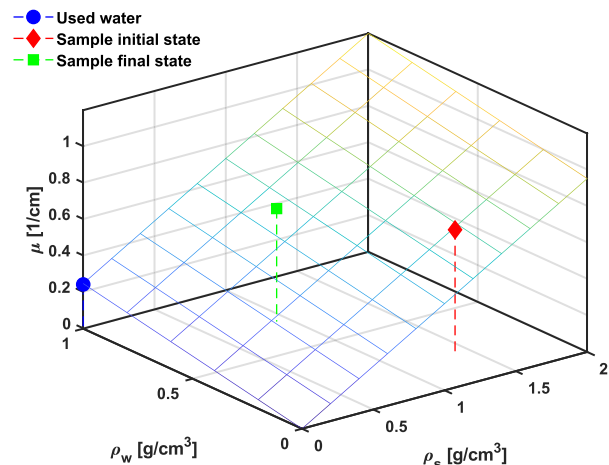

Fig. 2. Calibration fit from experiment E1. The fit (planar grid) yielded the mass attenuation coefficients of solid and water according to Eq. (2).

the sample in the final state and 3) the water used in the experiment (water filled sample chamber, $\rho_s = 0$). The approximate linearity was previously verified for the bentonite-water mixture in a wider range of partial densities (Harjupatana et al., 2015).

2.6. Measurement procedure

X-ray radiography was carried out using a SkyScan 1172 micro-tomographic scanner, which is designed for high-resolution 3D imaging, but can be used in X-ray radiography with minimal modifications. In this work, the microfocus X-ray tube of the scanner was operated using a tube voltage of 100 kV and a tube current of 80 μA. To reduce the effect of beam hardening and to increase transmittance, the lower part of the energy spectrum was cut using 0.5 mm aluminium and 0.04 mm copper filter plates. The image size of a single radiograph was 2000 (H) × 1048 (V) pixels (H = horizontal and V = vertical) with a pixel size of 17.1 μm, corresponding to a field of view of around 34 mm (H) × 18 mm (V). The exposure time was 4130 ms, and each radiograph was formed as an average of 18 exposures to improve the signal-to-noise ratio. The field of view was extended to 34 mm (H) × 30 mm (V) by stitching together three partly overlapping radiographs taken at different vertical positions. Three correction radiographs of background and 8 mm and 16 mm aluminium plates in the step wedge were also taken and used to correct the radiographs of the sample using the local beam hardening correction before stitching. The total acquisition time for a stitched and fully corrected radiograph was around 22 min. All the movement procedures in addition to acquiring and saving radiographs were automated with a computer script. Fig. 3 shows examples of corrected and stitched radiographs in the course of the 16-day wetting and swelling period.

The detailed measurement procedure, which encompasses the sample wetting process, is shown in Table 3. The sample was first radiographed in the initial state, after which wetting was started by introducing water into the sample chamber. Stage 1 A recorded the initial fast swelling and stage 1B the slower free swelling and transition to the constrained swelling. To capture the fast initial swelling in stages 1 A and 1B, the radiograph acquisition time was reduced from 22 min to 1.5 min and 3.9 min, respectively, by omitting most of the correction radiographs and decreasing the number of exposures used in averaging. Stages 2–9 were executed at increasing intervals as they monitored

Table 3

Measurement procedure. The number of stitched radiographs given includes the number of averaged radiographs and correction radiographs.

Stage	Time since water introduction	Number of stitched radiographs	Acquisition time per stitched radiograph [min]	State of sample
Initial	−30 min	1	22	Initial state
1 A	0 h	10	1.5	Start of wetting, fast initial free swelling
1B	15 min	40	3.9	Slower free swelling and transition to constrained swelling
2–8	3 h, 6 h, 12 h, 1 d, 2 d, 4 d, 8 d	7	22	Constrained swelling
9	16 d	1	22	Fully saturated final state

mainly the slow constrained swelling and saturation process. At the end of the wetting cycle (stage 9), the sample was removed from the sample chamber and weighed immediately, and again after 24-h oven drying at 105 °C to find out the mass of absorbed water, the dry mass and the mass of accumulated salt (i.e. dry mass gain between the final and initial states). The average dry density in the final state, used in density calibration (Sect. 2.5), was calculated using the dry mass and the dimensions of the sample. The dimensions were measured from the corresponding radiograph. To produce data for method validation, five samples were cut into horizontal slices of thickness 2–4 mm after the experiments. The partial densities of solid and water in the slices were determined using the gravimetric method (oven drying at 105 °C for 24 h) and the dimensions of the slices.

The radiographic method and the swelling pressure measurement produced the following data sets:

- deformation (positions of layer boundaries), $x_j(t)$
- partial density of solid (dry density), $\rho_s(x_j, t)$
- partial density of water, $\rho_w(x_j, t)$
- partial density of water at full saturation (saturation limit), $\rho_{w,\text{sat}}(x_j, t)$
- swelling pressure at both ends, $p_{\text{top}}(t)$ and $p_{\text{bottom}}(t)$.

All the results are available at Tanttu et al. (2023) and only selected results are presented below.

3. Results and discussion

3.1. Deformation

Fig. 4 shows the deformation of two samples, one from low salinity experiment E1 and the other from high salinity experiment E3. As the results are very different, it is evident that the salinity of the water strongly affects the swelling behaviour. In experiment E1, effectively only the topmost layers were swelling initially and the layers below were almost unchanged. In experiment E3, the swelling was much faster and also the lower layers were initially swelling. This indicates that the water transport rate increases with salinity. The rest of the deformation results can be found in Supplementary Material Sect. A. Overall, the repeatability of the deformation measurement was good, as replica measurements of the same experiment configuration gave consistent results. In the experiments where medium or high salinity solution was used, the typical time scale of the initial free expansion from the axial length 10 mm to 14 mm was a few minutes. In low salinity experiments
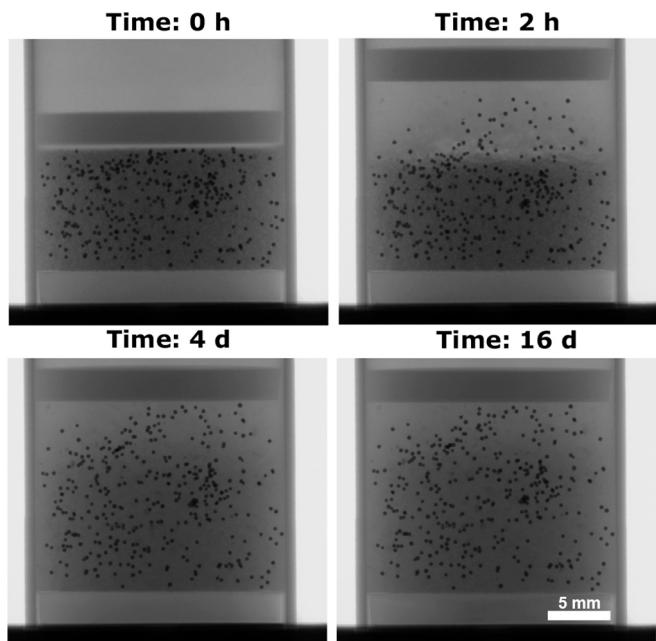

Fig. 3. Stitched radiographs from experiment E1 at four instants of time. The dark dots are the added ZrO_2 spheres.
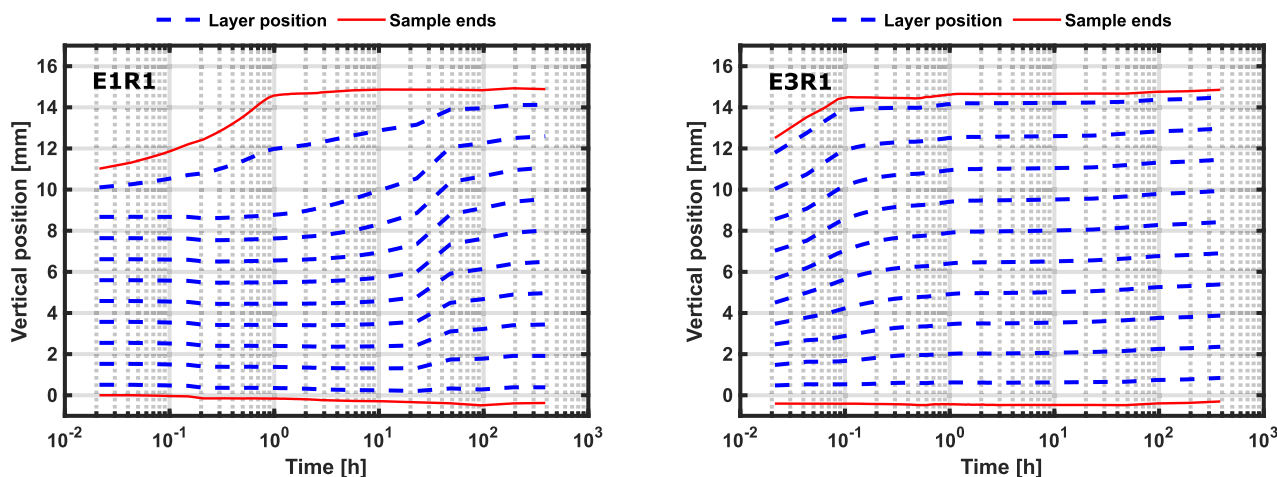
Fig. 4. Deformation of low density (1.4 g/cm³) CWB (Commercial Wyoming Bentonite) sample from low salinity experiment E1 (left) and high salinity experiment E3 (right). Layer position refers to the middle point between the layer boundaries. Notice that the initial state ($t = 0$, $h = 10$ mm) is not visible due to the logarithmic time axis.

instead, the typical time for such expansion was 1–3 h. High salinity experiment E9 deviated from this trend as the free expansion happened in 6–30 min.

The initial swelling rates for all the experiments are shown in Table 4. The swelling rates between the medium and high salinity experiments were similar but much higher than in the low salinity experiments. Again the only clear exception to this overall trend was experiment E9 where calcium montmorillonite was wetted with high salinity calcium solution. Both PCM experiments (E9 and E10) exhibited the largest spread in the initial swelling rates between the replicates, as indicated by the standard deviation. In the case of experiment E9, this variation could potentially be attributed to the interaction between aqueous calcium in the wetting solution and atmospheric carbon dioxide during storage. This interaction may reduce the salinity of the solution through the formation of calcium carbonate precipitate (Broadley et al., 2008). However, no significant changes in pH or visible precipitation were observed during the experiment. In contrast, in the case of experiment E10, the presence of precipitates cannot account for the observed variability, as the salinity of the wetting solution was so low. Therefore, these findings suggest that the significant spread in the initial swelling rates is likely associated with the properties of the PCM material itself or potential measurement anomalies rather than the characteristics of the wetting solution. It should be noted that in PSM and PCM experiments the initial water content was higher than in the CWB experiment as discussed in Sect. 2.1 and shown in Table 2. The initial water content affects the swelling capacity of compacted bentonite as indicated by Villar and Lloret (2008) and Harjupatana et al. (2022). Evaluating how this affects the swelling in the present study is difficult

as the materials and the wetting solutions differed between the experiments.

To compare the behaviour of the initial free swelling phase to previous studies, Sane et al. (2013) and Navarro et al. (2017) conducted free swelling experiments and observed a similar trend as was seen here, the swelling rate increased with salinity. Similarly, to what is seen in the swelling rates measured here, Navarro et al. (2017) reported that there is no significant difference between swelling experiments with salinities of approximately 0.8 M and 1.5 M. However, an exact quantitative comparison of these results is again challenging as their measurement set-ups were different from that of the present study.

3.2. Partial densities

Examples of measured partial density profiles of bentonite and water together with saturation limits at different instants of time from experiment E1 are shown in Fig. 5. Also plotted are the gravimetric validation data from the sliced sample in the final state (16 d). The error bars are the standard deviations of all three replicates. The results are within the error bars in all positions except near 0.8 cm, which seems to be an outlier, and near 0.2 cm, where the measurements deviate slightly. Overall, the results given by the radiographic method seem to agree relatively well with the gravimetric validation data. The results of the rest experiments with validation data can be found in Supplementary Material Sect. B. Although this sample was wetted with low salinity solution and the water transport was thus slow, it seems that the sample was fully saturated already in four days. The density gradient found at 4 d remains approximately the same in the final state (16 d) indicating that the homogenisation process stopped or was progressing very slowly.

To further investigate the homogenisation, Fig. 6 shows water content and dry density profiles in the final state from experiments E1 and E3. Similar plots for the rest of the experiments can be found in Supplementary Material Sect. C. In general, the repeatability of the experiments was good as the final state dry density and water content profiles of the replicates are similar. When comparing the profiles along the sample length, it can be seen that the water in high salinity experiment E3 distributed more evenly across the sample. Additionally, the dry density distribution seems to be more homogeneous in experiment E3. However, none of the experiments reached the fully homogeneous state after 16 days of wetting and swelling. Similar heterogeneous results in comparable void swelling experiments were observed in previous studies, as was discussed in Sect. 1. While direct quantitative comparisons to past research are not feasible due to variations in experimental
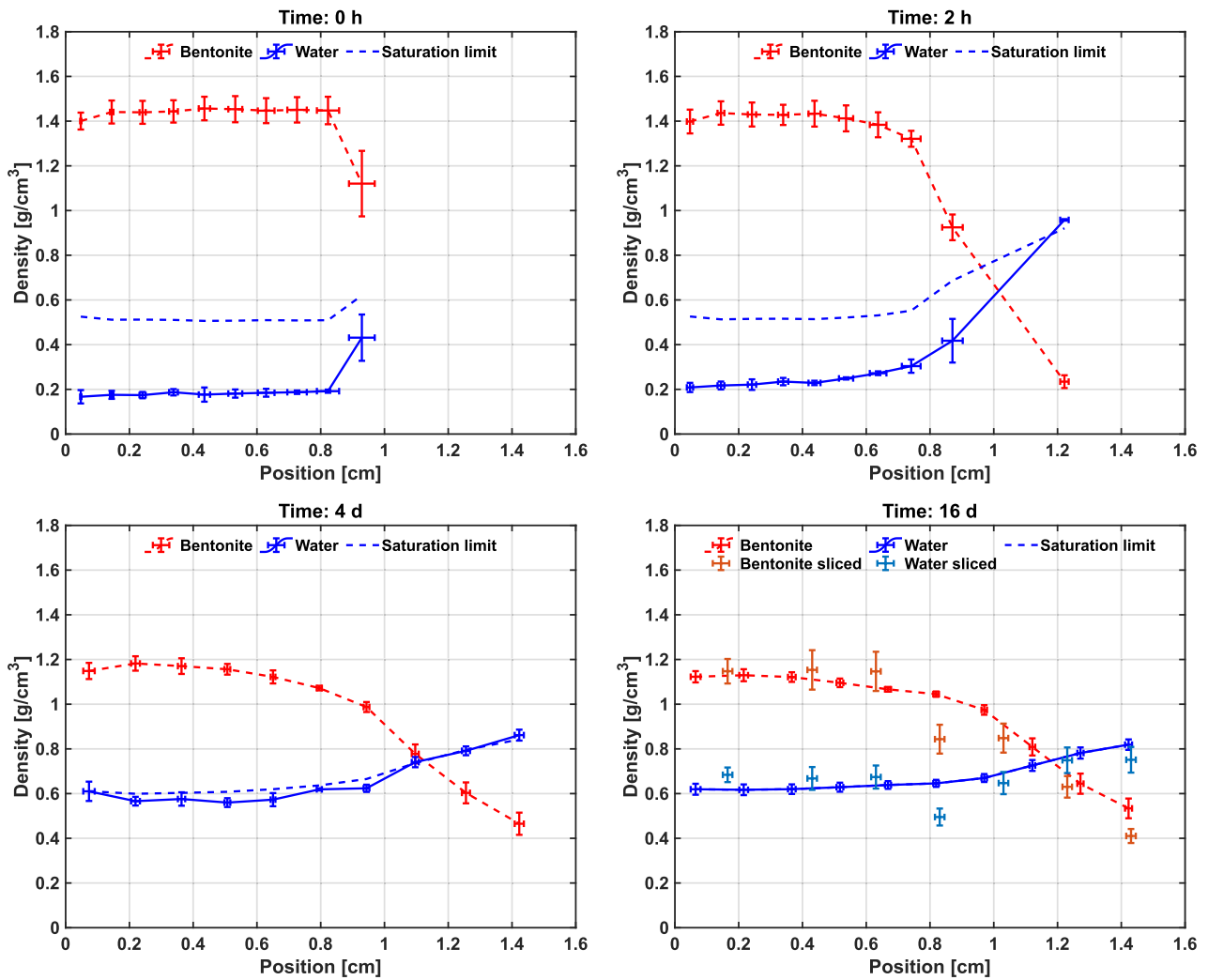
Table 4

Initial swelling rate for each experiment. The initial swelling rate was calculated from the movement of the top surface during the first 5 min of swelling and is given here as the mean ± standard deviation of the three replicates.

Exp. ID	Material	Initial dry density [g/cm³]	Ionic strength [mM]	Initial swelling rate [mm/min]
E1	CWB	1.4	3.5	0.44 ± 0.02
E2	CWB	1.4	489	1.40 ± 0.12
E3	CWB	1.4	975	1.35 ± 0.11
E4	CWB	1.8	3.5	0.24 ± 0.09
E5	CWB	1.8	489	1.20 ± 0.03
E6	CWB	1.8	975	1.05 ± 0.09
E7	PSM	1.4	975	1.72 ± 0.10
E8	PSM	1.8	3.5	0.22 ± 0.04
E9	PCM	1.4	975	0.45 ± 0.26
E10	PCM	1.8	3.5	0.22 ± 0.18

Fig. 5. Examples of the main results from experiment E1. The partial density profiles of and water are shown at four instants of time. Also shown are the saturation limits (Eq. (7)), i.e. the maximum amount of water the sample can hold. The gravimetric validation data from the sliced sample are shown in the final state (16 d). The error bars of the partial densities are the standard deviations of the three replicates, and the error bars of the validation data were obtained by estimating the errors in the slicing and weighing procedures.
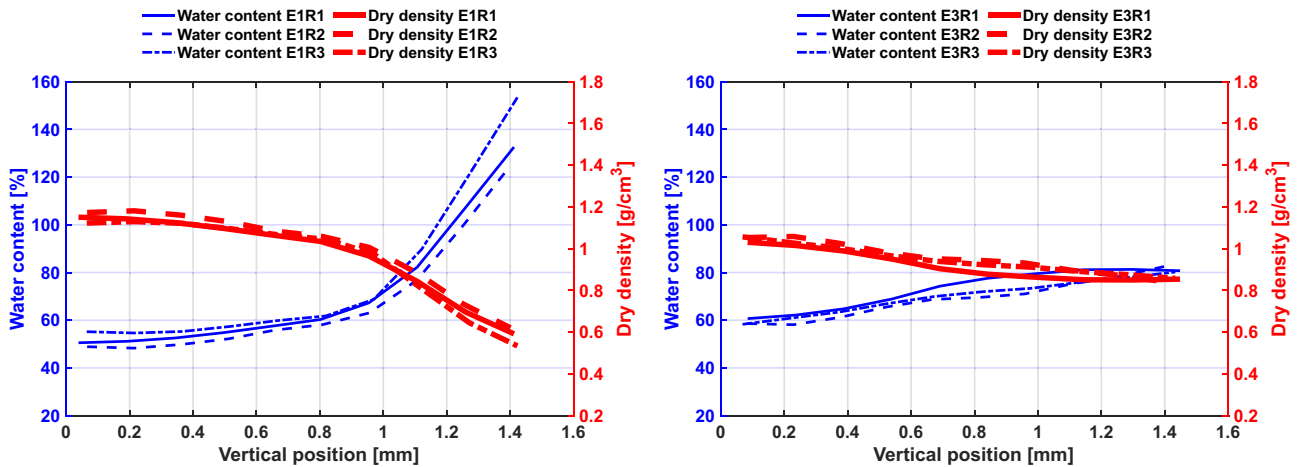

Fig. 6. Final state water content and dry density profiles from low salinity experiment E1 (left) and high salinity experiment E3 (right).

set-ups and parameters, the qualitative analysis of the gathered results aligns with past research. Most notably, the dry density and water content profiles exhibit similar trends. The wetting end of the sample has a higher water content and a lower dry density in the final state.

As the partial density analysis requires the calibration of Eq. (2), one could argue that the equation does not hold for medium and high salinity solutions as the salt from the solution can accumulate and remain in the structure of the sample. This is a valid point as the weighing results shown in Table 5 indicate that the dry masses of the samples increased more than expected, suggesting significant salt accumulation within them. This accumulation may be attributed to the flow of water through the samples, leaving excess salt behind. Additionally, the accumulated salt may have bound water into its crystalline structure, which was not removed even at 105 °C. Unfortunately, the reason for the mass gain could not be clarified, and further investigation is required. Significant salt accumulation might affect the now obtained final dry density distributions in high salinity experiments as accumulated salt could result in increased dry density. It would be particularly important to know where the salt is locally situated to estimate its effect on the results. If salt accumulates more on top of the sample (i.e. wetting end), it might also contribute to the seemingly more homogeneous final state dry density and water content profiles in high salinity experiments. In the forward analysis (see Sect. 2.3), only the initial state dry density distribution and the measured deformation are used to calculate the final state dry density distribution, and hence the result is not affected by salt accumulation. As the final state dry density profiles calculated using both the forward analysis and the backward analysis (currently used for the final state) have similar trends (Supplementary Material Sect. F), it seems that the salt is evenly distributed rather than locally accumulated in certain places. However, further research and method development are needed to study salt accumulation in more detail. Separating the LAC of solid phase to dry clay and different salt components and measuring them separately would require, e.g. advanced energy-sensitive imaging techniques to differentiate materials by their spectral characteristics (Alessio and MacDonald, 2013). Another common practice which could be employed in future studies for measuring salinity changes in clay material is aqueous extraction (Aschwanden et al., 2024). This method can be applied to individual slices of the sample to assess the local variations in salinity.

Fig. 7 shows the temporal evolution of water content at two different vertical positions of samples. Similar plots for all the replicates can be found in Supplementary Material Sect. D. water content development in different layers gives further perspective on the water transport rate and the homogenisation process. It can be seen that the initial response to water intrusion and saturation rate was very different between the low salinity experiments (E1, E4, E8 and E10), and the medium and high salinity experiments (E2, E3, E5, E6, E7 and E9). In the medium and high salinity experiments, the initial saturation rate was fast throughout the sample as the water permeated the top layer more efficiently and

distributed more evenly into the sample than in the low salinity experiments. This can be observed as a significant difference in the water content between the top and middle layers of experiments E1, E4, E8, and E10, as shown in Fig. 7. In the low salinity experiments, water built up at the top of the sample, forming an apparently weakly permeable layer that slowed the water transport and thus the overall homogenisation process. High salinity experiment E9 was again a clear exception to this trend as the water did not initially permeate deeper into the sample. The explanation for this phenomenon could be similar to that discussed in Sect. 3.1. However, it is plausible that the observed phenomena are related to attributes of the PCM material, as indicated in Supplementary Material Sect. D, where there is also variation in the behaviour of experiment E10. Thus, further study is required to validate this behaviour, as there is currently no reference material in the literature.

3.3. Swelling pressure

Swelling pressure plots for all the samples can be found in Supplementary Material Sect. E. Fig. 8 shows examples of swelling pressures from experiment E1. In this experiment, the general trend was similar between the replicates but the values varied. The differences between the top and bottom end swelling pressure values were likely caused by wall friction. These values, shown in Fig. 8 (right) seem to converge to the same value after the initial deviation. The wall friction may be more sensitive to density variations when the sample is relatively dry in the initial state. In some experiments, the bottom end swelling pressure values collapsed after the initial rapid increase, after which the values developed towards the final saturation values. This event might be explained by a combination of wall friction and structural changes during water transport and swelling.

The measurements indicate that the ionic strength of the solution affects the swelling pressure of bentonite. This is further elaborated in Table 6 where the final state swelling pressures (average of both ends) and the final state swelling pressure differences in the experiment are shown. It seems that the swelling pressure decreases with the salinity of the solution, which is in agreement with past research (Karnland et al., 2006). Furthermore, higher initial dry density seems to lead to higher swelling pressures, which is also to be expected according to Karnland et al. (2006) and Dueck et al. (2019). All the swelling pressure values were relatively small due to the low dry density in the final state (1.0–1.3 g/cm^3). Because of these effects, the swelling pressures of the low density CWB samples were negligible in medium and high salinity experiments E2 and E3, which is in agreement with Daniels et al. (2021). Also, the swelling pressure difference seems to slightly decrease with the salinity of the solution. The difference was larger for the experiments where the initial dry density was higher, indicating that wall friction was more dominant in these experiments.

When comparing PCM experiments to their CWB counterparts, it can be seen that PCM experiments E9 and E10 exhibited slightly higher or similar final swelling pressures as CWB experiments E3 and E4. On the other hand, PSM experiment E8 shows that by increasing the sodium montmorillonite content, higher swelling pressures can be achieved compared to CWB experiment E4, which is in line with the results found by Karnland et al. (2006). The low swelling pressure in experiment E7 compared to experiment E8 shows again the effects of the initial dry density and the salinity of the solution on the swelling pressure.

4. Conclusions

In this study, X-ray radiography and numerical image analysis were used to quantify the fast wetting and swelling process of different clay materials. The measurement method was shown to be able to collect time evolution data on one-dimensional solid material deformation and water content distribution without damaging the sample.

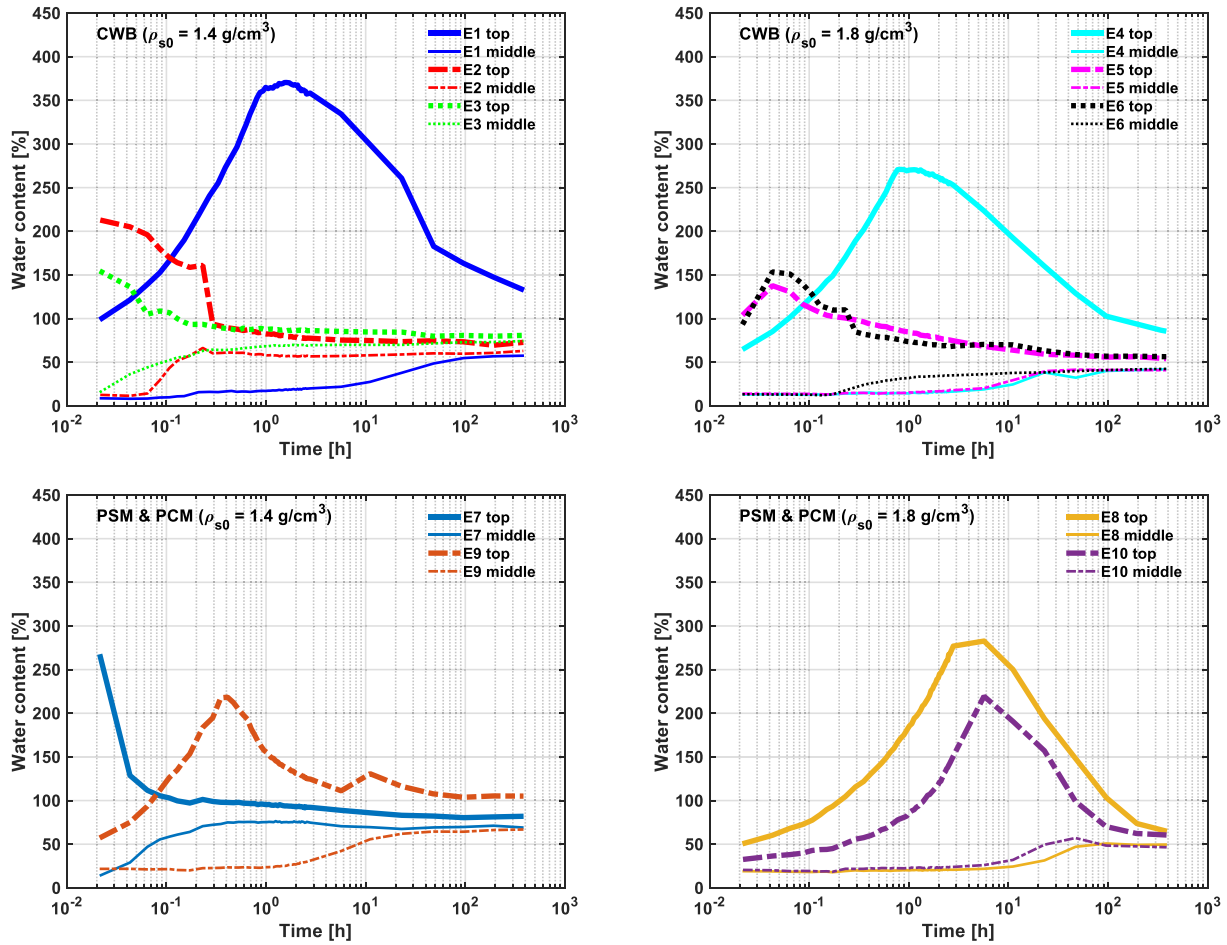The deformation analysis revealed significant differences in the

Table 5
Accumulation of salt in samples in the experiments. The expected mass of salt is the mass of salt in the amount of water needed to fully saturate the sample. The dry mass gain is the difference between the final and initial state dry masses, given as the mean $\pm$ standard deviation of the three replicates.

Exp. ID	Ionic strength [mM]	Expected mass of salt [mg]	Dry mass gain [mg]
E1	3.5	0.4	25 ± 49
E2	489	52.2	132 ± 38
E3	975	104.0	237 ± 54
E4	3.5	0.3	5 ± 98
E5	489	37.1	141 ± 27
E6	975	73.9	139 ± 38
E7	975	111.9	343 ± 258
E8	3.5	0.3	-26 ± 211
E9	975	69.2	200 ± 114
E10	3.5	0.2	27 ± 18

Fig. 7. Time evolution of water content at two vertical positions of sample. Top refers to the topmost layer and middle to the fifth layer. Low salinity experiments are E1, E4, E8 and E10. Medium and high salinity experiments are E2, E3, E5, E6, E7 and E9.
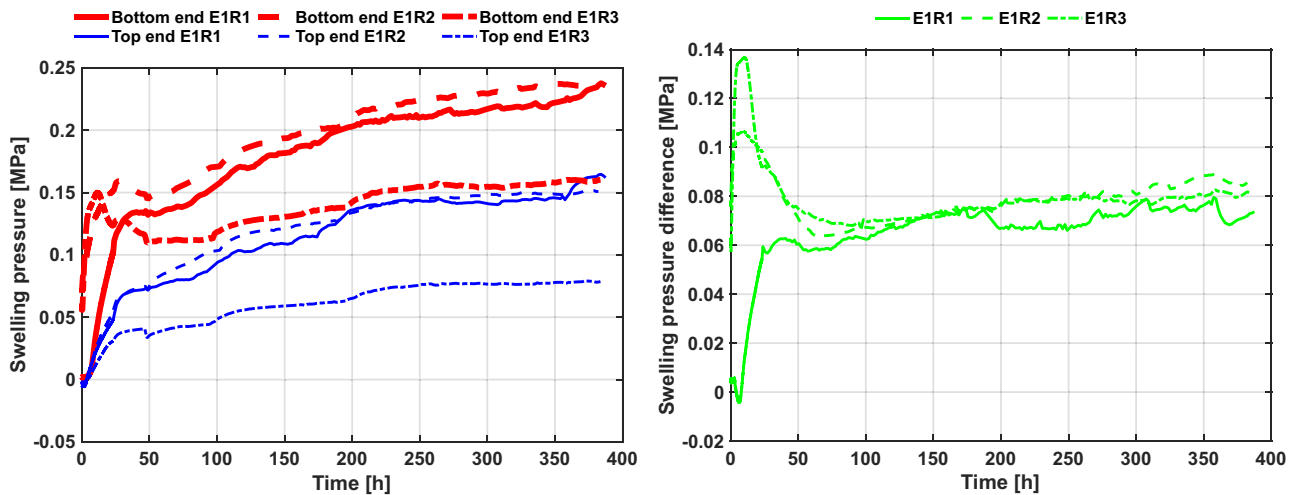

Fig. 8. Time development of swelling pressure (left) and swelling pressure difference $p_{bottom} - p_{top}$ (right) in experiment E1. Suffixes R1, R2 and R3 refer to the replicate number of the measurement.

swelling behaviour of the clay samples based on the salinity of the wetting solution. Higher salinity solutions resulted in faster swelling, while low salinity solutions exhibited swelling primarily in the topmost layers. These findings indicate that the water transport rate increases with salinity.

Analysis of partial densities provided crucial insights into the saturation and homogenisation processes. Despite the slow transport of water in low salinity experiments, efficient wetting and full saturation was achieved within a few days. The density gradients remained relatively stable throughout the wetting process, suggesting a slowdown or

Table 6
Average swelling pressure and swelling pressure difference between the top and the bottom ends of the sample in the final state. The values are calculated as $\left(p_{\text{bottom}}(t_f) + p_{\text{top}}(t_f) \right)/2$ and $p_{\text{bottom}}(t_f) - p_{\text{top}}(t_f)$, respectively. The error estimates are the standard deviations of the three replicates.

Exp. ID	Material	Initial dry density [g/cm^3]	Ionic strength [mM]	Final state swelling pressure [MPa]	Final state swelling pressure difference [MPa]
E1	CWB	1.4	3.5	0.17 ± 0.06	0.08 ± 0.01
E2	CWB	1.4	489	0.02 ± 0.01	0.01 ± 0.00
E3	CWB	1.4	975	0.00 ± 0.01	0.00 ± 0.01
E4	CWB	1.8	3.5	0.56 ± 0.13	0.20 ± 0.05
E5	CWB	1.8	489	0.30 ± 0.13	0.23 ± 0.01
E6	CWB	1.8	975	0.18 ± 0.11	0.15 ± 0.05
E7	PSM	1.4	975	0.10 ± 0.05	0.06 ± 0.02
E8	PSM	1.8	3.5	1.27 ± 0.30	0.29 ± 0.14
E9	PCM	1.4	975	0.11 ± 0.06	0.08 ± 0.02
E10	PCM	1.8	3.5	0.51 ± 0.16	0.23 ± 0.03

halt in the homogenisation process. Comparisons between experiments emphasised the influence of salinity on water and dry density distribution, with higher salinity solutions leading to a more homogeneous dry density profile. However, complete homogenisation was not achieved even after 16 days, consistent with similar studies and highlighting the complexity of the process.

As the dry mass of the samples systematically increased with the salinity of the wetting solution and the measured mass gains were higher than expected at the end of the experiments, significant salt accumulation likely occurred in the samples. Comparison of the final state dry density profiles, calculated using the forward and backward analysis, indicated that the salt is evenly distributed along the sample. However, more detailed studies on salt accumulation are needed to confirm this and to further study its effect on the swelling behaviour.

Swelling pressure analysis demonstrated the influence of ionic strength and initial dry density on the behaviour of the clay materials. Higher salinity solutions resulted in decreased swelling pressures, while higher initial dry densities led to increased pressures. Experiments with higher sodium montmorillonite content exhibited higher swelling pressures.

While the current study focused on measuring the variation of water content using X-ray radiography, future studies could benefit from further insights through the establishment of a soil-water retention curve (SWRC). The SWRC tests would involve wetting cylindrical test samples of the clay under different controlled suction conditions, mirroring the conditions of samples in this study. By measuring the volumetric water content at each suction level and fitting the data to an appropriate SWRC model, could potentially establish a relationship between water content and suction for specific clay material.

Although the results agree well with previous literature, there were some disadvantages to the X-ray radiography method. Fast swelling causes motion blur in the radiographs if the imaging speed is not sufficient. This can be well overcome by a specific optimised imaging protocol like the one used here. The deformation measurement requires that the sample contains details that are visible in the radiographs and that move along the deforming clay. To ensure this condition, small tracer particles were added to the samples. It was however hard to ensure their uniform distribution in the sample, and the non-uniform distribution may lead to varying resolution in the deformation analysis, in particular near the edges of the sample.

Despite the sources of inaccuracy, the method can produce data that agrees with available validation methods and literature. This study shows that the now modified X-ray-based method can be applied to measure rapid homogenisation processes involving water transport in solid materials where non-destructive spatio-temporal monitoring of deformation and water content is needed during the whole wetting

process. The method seems to be less cumbersome and faster than the traditional gravimetric slicing method and therefore provides a viable alternative to that. The consistent results between the replicates indicate that the swelling behaviour between them is similar but it also highlights the fact that the repeatability of the method is good.

CRediT authorship contribution statement

Joni Tanttu: Writing – original draft, Visualization, Software, Methodology, Investigation, Formal analysis. **Tero Harjupatana:** Writing – review & editing, Visualization, Software, Methodology, Investigation, Formal analysis. **Arttu Miettinen:** Writing – review & editing, Supervision, Project administration. **Markku Kataja:** Writing – review & editing, Supervision, Software, Project administration, Methodology, Funding acquisition, Formal analysis.

Declaration of competing interest

The authors declare that they have no known competing financial interests or personal relationships that could have appeared to influence the work reported in this paper.

Data availability

The data is available at 10.5281/zenodo.7691488

Acknowledgements

Appendix A. Supplementary data

Supplementary data to this article can be found online at https://doi.org/10.1016/j.clay.2024.107443.

References

Alaoui, A., Lipiec, J., Gerke, H., 2011. A review of the changes in the soil pore system due to soil deformation: a hydrodynamic perspective. Soil Tillage Res. 115, 1–15.

Alessio, A.M., MacDonald, L.R., 2013. Quantitative material characterization from multi-energy photon counting CT. Med. Phys. 40 (3), 031108.

Aschwanden, L., Wersin, P., Debure, M., Traber, D., 2024. Experimental study of water-extractable sulphate in Opalinus Clay and implications for deriving porewater concentrations. Appl. Geochem. 160, 105837.

Broadley, S., Vondrak, T., Wright, T.G., Plane, J.M., 2008. A kinetic study of Ca-containing ions reacting with O, O2, CO2 and H2O: implications for calcium ion chemistry in the upper atmosphere. Phys. Chem. Chem. Phys. 10 (34), 5287–5298.

Daniels, K., Harrington, J., Sellin, P., Norris, S., 2021. Closing repository void spaces using bentonite: does heat make a difference? Applied Clay Science 210, 106124.

Daniels, K., Graham, C., Wiseall, A., Harrington, J., Sellin, P., 2024. Bentonite homogenisation and swelling: the effect of salinity. Applied Clay Science 247, 107200.

Dueck, A., Börgesson, L., Kristensson, O., Malmberg, D., Kesson, M., Hernelind, J., 2019. Bentonite Homogenisation. Laboratory Study, Model Development and Modelling of Homogenisation Processes. Technical Report TR-19-11. SKB.

Fanta, S.W., Abera, M.K., Aregawi, W.A., Ho, Q.T., Verboven, P., Carmeliet, J., Nicolai, B. M., 2014. Microscale modeling of coupled water transport and mechanical deformation of fruit tissue during dehydration. J. Food Eng. 124, 86–96.

Gardner, W.H., 1986. Water content. Methods of Soil Analysis: part 1 Physical and Mineralogical. Methods 5, 493–544.

Gummerson, R., Hall, C., Hoff, W., Hawkes, R., Holland, G., Moore, W., 1979. Unsaturated water flow within porous materials observed by NMR imaging. Nature 281 (5726), 56–57.

Harjupatana, T., Alaraudanjoki, J., Kataja, M., 2015. X-ray tomographic method for measuring three-dimensional deformation and water content distribution in swelling clays. Applied Clay Science 114, 386–394.

Harjupatana, T., Miettinen, A., Kataja, M., 2022. A method for measuring wetting and swelling of bentonite using X-ray imaging. Appl. Clay Sci. 221, 106485.

Karnland, O., Olsson, S., Nilsson, U., 2006. Mineralogy and Sealing Properties of Various Bentonites and Smectite-Rich Clay Materials. Technical Report TR-06-30. SKB.

Karnland, O., Nilsson, U., Weber, H., Wersin, P., 2008. Sealing ability of Wyoming bentonite pellets foreseen as buffer material–laboratory results. Physics and Chemistry of the Earth, Parts A/B/C 33, S472–S475.

Kiviranta, L., Kumpulainen, S., 2011. Quality Control and Characterization of Bentonite Materials. Technical Report 2011-84. Posiva Oy.

Kröhn, K.-P., 2019. Re-saturation of compacted bentonite under repository-relevant flow conditions. Geomechanics for Energy and the Environment 17, 115–122.

Markgraf, W., Horn, R., Peth, S., 2006. An approach to rheometry in soil mechanics—structural changes in bentonite, clayey and silty soils. Soil and Tillage Research 91 (1–2), 1–14.

Navarro, V., Yustres, Á., Asensio, L., De la Morena, G., González-Arteaga, J., Laurila, T., Pintado, X., 2017. Modelling of compacted bentonite swelling accounting for salinity effects. Eng. Geol. 223, 48–58.

Nizovtsev, M., Stankus, S., Sterlyagov, A., Terekhov, V., Khairulin, R., 2008. Determination of moisture diffusivity in porous materials using gamma-method. Int. J. Heat Mass Transf. 51 (17–18), 4161–4167.

Pereira, C.G., Castro-Gomes, J., de Oliveira, L.P., 2009. Influence of natural coarse aggregate size, mineralogy and water content on the permeability of structural concrete. Construct. Build Mater. 23 (2), 602–608.

Sane, P., Laurila, T., Olin, M., Koskinen, K., 2013. Current Status of Mechanical erosion Studies of Bentonite Buffer. Technical Report 2012-45. Posiva Oy.

Tanttu, J., Harjupatana, T., Miettinen, A., Kataja, M., 2023. BEACON project data. Zenodo. https://doi.org/10.5281/zenodo.7691488.

Tippkötter, R., Eickhorst, T., Taubner, H., Gredner, B., Rademaker, G., 2009. Detection of soil water in macropores of undisturbed soil using microfocus X-ray tube computerized tomography (μCT). Soil and Tillage Research 105 (1), 12–20.

Villar, M.V., Lloret, A., 2008. Influence of dry density and water content on the swelling of a compacted bentonite. Applied Clay Science 39 (1–2), 38–49.

Villar, M.V., Gutiérrez-Álvarez, C., Campos, G., 2023. Bentonite swelling into a void under suction or water flow. Acta Geotech. 18 (3), 1495–1513.

Wildenschild, D., Sheppard, A.P., 2013. X-ray imaging and analysis techniques for quantifying pore-scale structure and processes in subsurface porous medium systems. Adv. Water Resour. 51, 217–246.

Ye, W.-M., Chen, Y.-G., Chen, B., Wang, Q., Wang, J., 2010. Advances on the knowledge of the buffer/backfill properties of heavily-compacted GMZ bentonite. Engineering Geology 116 (1–2), 12–20.

Yustres, A., Jenni, A., Asensio, L., Pintado, X., Koskinen, K., Navarro, V., Wersin, P., 2017. Comparison of the hydrogeochemical and mechanical behaviours of compacted bentonite using different conceptual approaches. Applied Clay Science 141, 280–291.

Zhang, P., Wittmann, F.H., Zhao, T.-J., Lehmann, E.H., Vontobel, P., 2011. Neutron radiography, a powerful method to determine time-dependent moisture distributions in concrete. Nucl. Eng. Des. 241 (12), 4758–4766.